

# The asymmetry of antimatter in the proton

<https://doi.org/10.1038/s41586-021-03282-z>

Received: 2 June 2020

Accepted: 15 December 2020

Published online: 24 February 2021

 Check for updates

J. Dove<sup>1</sup>, B. Kerns<sup>1</sup>, R. E. McClellan<sup>1,18</sup>, S. Miyasaka<sup>2</sup>, D. H. Morton<sup>3</sup>, K. Nagai<sup>2,4</sup>, S. Prasad<sup>1</sup>, F. Sanftl<sup>2</sup>, M. B. C. Scott<sup>3</sup>, A. S. Tadepalli<sup>5,18</sup>, C. A. Aidala<sup>3,6</sup>, J. Arrington<sup>7,19</sup>, C. Ayuso<sup>3,20</sup>, C. L. Barker<sup>8</sup>, C. N. Brown<sup>9</sup>, W. C. Chang<sup>4</sup>, A. Chen<sup>1,3,4</sup>, D. C. Christian<sup>10</sup>, B. P. Dannowitz<sup>1</sup>, M. Daugherty<sup>8</sup>, M. Diefenthaler<sup>1,18</sup>, L. El Fassi<sup>5,11</sup>, D. F. Geesaman<sup>7,21</sup>, R. Gilman<sup>5</sup>, Y. Goto<sup>12</sup>, L. Guo<sup>6,22</sup>, R. Guo<sup>13</sup>, T. J. Hague<sup>8</sup>, R. J. Holt<sup>7,23</sup>, D. Isenhower<sup>8</sup>, E. R. Kinney<sup>14</sup>, N. Kitts<sup>8</sup>, A. Klein<sup>6</sup>, D. W. Kleinjan<sup>6</sup>, Y. Kudo<sup>15</sup>, C. Leung<sup>1</sup>, P.-J. Lin<sup>14</sup>, K. Liu<sup>6</sup>, M. X. Liu<sup>6</sup>, W. Lorenzon<sup>3</sup>, N. C. R. Makins<sup>1</sup>, M. Mesquita de Medeiros<sup>7</sup>, P. L. McGaughey<sup>6</sup>, Y. Miyachi<sup>15</sup>, I. Mooney<sup>3,24</sup>, K. Nakahara<sup>16,25</sup>, K. Nakano<sup>2,12</sup>, S. Nara<sup>15</sup>, J.-C. Peng<sup>1</sup>, A. J. Puckett<sup>6,26</sup>, B. J. Ramson<sup>3,27</sup>, P. E. Reimer<sup>7,28</sup>, J. G. Rubin<sup>3,7</sup>, S. Sawada<sup>17</sup>, T. Sawada<sup>3,28</sup>, T.-A. Shibata<sup>2,29</sup>, D. Su<sup>4</sup>, M. Teo<sup>1,30</sup>, B. G. Tice<sup>7</sup>, R. S. Towell<sup>8</sup>, S. Uemura<sup>6,31</sup>, S. Watson<sup>8</sup>, S. G. Wang<sup>4,13,32</sup>, A. B. Wickes<sup>6</sup>, J. Wu<sup>10</sup>, Z. Xi<sup>8</sup> & Z. Ye<sup>7</sup>

The fundamental building blocks of the proton—quarks and gluons—have been known for decades. However, we still have an incomplete theoretical and experimental understanding of how these particles and their dynamics give rise to the quantum bound state of the proton and its physical properties, such as its spin<sup>1</sup>. The two up quarks and the single down quark that comprise the proton in the simplest picture account only for a few per cent of the proton mass, the bulk of which is in the form of quark kinetic and potential energy and gluon energy from the strong force<sup>2</sup>. An essential feature of this force, as described by quantum chromodynamics, is its ability to create matter–antimatter quark pairs inside the proton that exist only for a very short time. Their fleeting existence makes the antimatter quarks within protons difficult to study, but their existence is discernible in reactions in which a matter–antimatter quark pair annihilates. In this picture of quark–antiquark creation by the strong force, the probability distributions as a function of momentum for the presence of up and down antimatter quarks should be nearly identical, given that their masses are very similar and small compared to the mass of the proton<sup>3</sup>. Here we provide evidence from muon pair production measurements that these distributions are considerably different, with more abundant down antimatter quarks than up antimatter quarks over a wide range of momenta. These results are expected to revive interest in several proposed mechanisms for the origin of this antimatter asymmetry in the proton that had been disfavoured by previous results<sup>4</sup>, and point to future measurements that can distinguish between these mechanisms.

The structure of the proton is a prototypical example of a strongly coupled and correlated system with quarks and gluons interacting according to quantum chromodynamics (QCD). At large energy and momentum scales, the interaction is relatively weak, whereas at lower energy scales the picture is clouded by the increasingly strong

interaction. The original quark model, in which the proton consists of two up quarks (*u*) and one down (*d*) quark, has an appealing simplicity, but experiments that measure the distributions of quarks as a function of the fractional momentum (*x*) of the proton that these quarks carry have revealed a rich structure with additional quarks, antimatter quarks

<sup>1</sup>Department of Physics, University of Illinois at Urbana-Champaign, Urbana, IL, USA. <sup>2</sup>Department of Physics, School of Science, Tokyo Institute of Technology, Tokyo, Japan. <sup>3</sup>Randall Laboratory of Physics, University of Michigan, Ann Arbor, MI, USA. <sup>4</sup>Institute of Physics, Academia Sinica, Taipei, Taiwan. <sup>5</sup>Department of Physics and Astronomy, Rutgers, The State University of New Jersey, Piscataway, NJ, USA. <sup>6</sup>Physics Division, Los Alamos National Laboratory, Los Alamos, NM, USA. <sup>7</sup>Physics Division, Argonne National Laboratory, Lemont, IL, USA. <sup>8</sup>Department of Engineering and Physics, Abilene Christian University, Abilene, TX, USA. <sup>9</sup>Accelerator Division, Fermi National Accelerator Laboratory, Batavia, IL, USA. <sup>10</sup>Particle Physics Division, Fermi National Accelerator Laboratory, Batavia, IL, USA. <sup>11</sup>Department of Physics and Astronomy, Mississippi State University, Mississippi State, MS, USA. <sup>12</sup>RIKEN Nishina Center for Accelerator-Based Science, Wako, Japan. <sup>13</sup>Department of Physics, National Kaohsiung Normal University, Kaohsiung, Taiwan. <sup>14</sup>Department of Physics, University of Colorado, Boulder, CO, USA. <sup>15</sup>Department of Physics, Yamagata University, Yamagata, Japan. <sup>16</sup>Department of Physics, University of Maryland, College Park, MD, USA. <sup>17</sup>Institute of Particle and Nuclear Studies, KEK, High Energy Accelerator Research Organization, Tsukuba, Japan. <sup>18</sup>Present address: Experimental Nuclear Physics Division, Thomas Jefferson National Accelerator Facility, Newport News, VA, USA. <sup>19</sup>Present address: Physics Division, Lawrence Berkeley National Laboratory, Berkeley, CA, USA. <sup>20</sup>Present address: Department of Physics, Mississippi State University, Mississippi State, MS, USA. <sup>21</sup>Present address: Global Empire LLC, Lemont, IL, USA. <sup>22</sup>Present address: Department of Physics, Florida International University, Miami, FL, USA. <sup>23</sup>Present address: Kellogg Radiation Laboratory, California Institute of Technology, Pasadena, CA, USA. <sup>24</sup>Present address: Department of Physics, Wayne State University, Detroit, MI, USA. <sup>25</sup>Present address: Stanford Linear Accelerator Center, Menlo Park, CA, USA. <sup>26</sup>Present address: Department of Physics, University of Connecticut, Storrs, CT, USA. <sup>27</sup>Present address: Neutrino Division, Fermi National Accelerator Laboratory, Batavia, IL, USA. <sup>28</sup>Present address: Department of Physics, Osaka City University, Osaka City, Japan. <sup>29</sup>Present address: Department of Physics, College of Science and Technology, Nihon University, Tokyo, Japan. <sup>30</sup>Present address: Department of Physics, Stanford University, Stanford, CA, USA. <sup>31</sup>Present address: Department of Physics, Tel Aviv University, Tel Aviv, Israel. <sup>32</sup>Present address: Accelerator Systems Division, Argonne National Laboratory, Lemont, IL, USA. <sup>✉</sup>e-mail: reimer@anl.gov

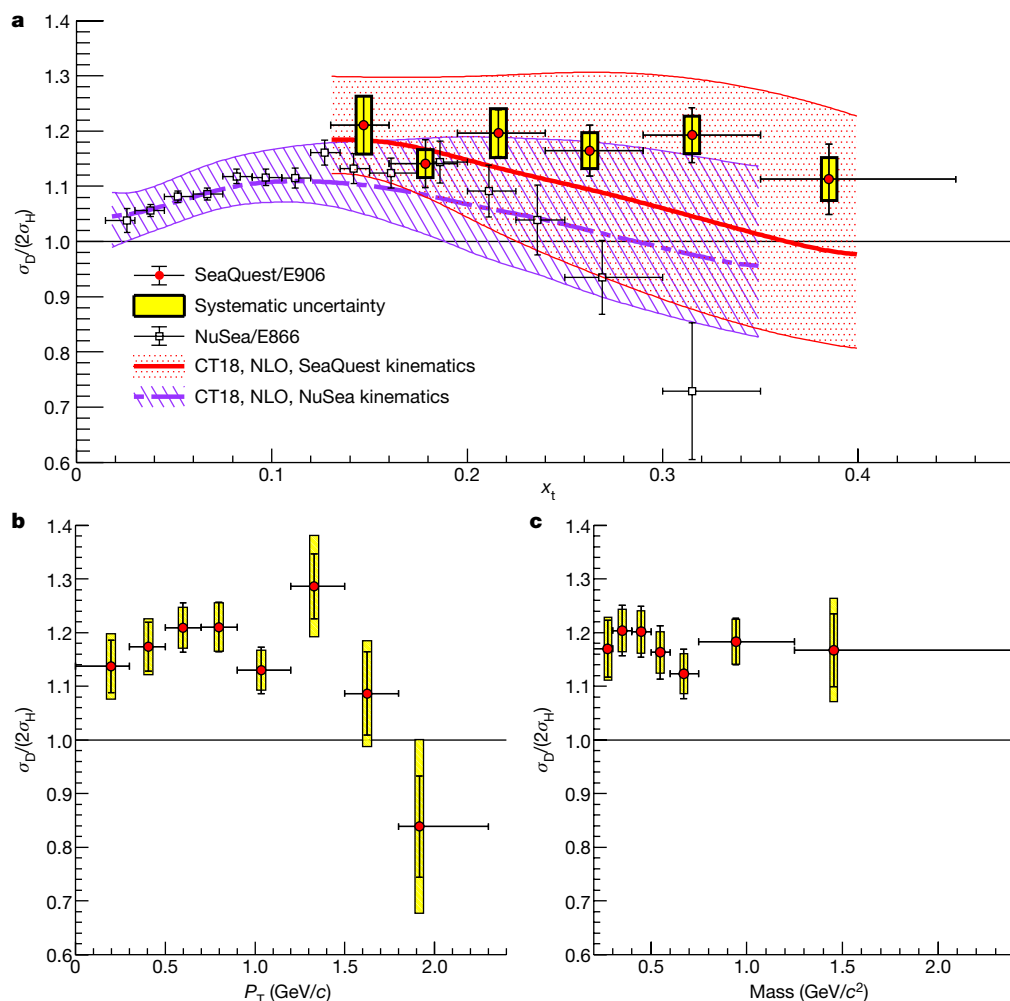


**Fig. 1 | Ratios  $\sigma_D/(2\sigma_H)$ .** **a–c**, Ratios  $\sigma_D(x_t)/[2\sigma_H(x_t)]$  (red filled circles) with their statistical (vertical bars) and systematic (yellow boxes) uncertainties as a function of  $x_t$  (**a**) and of transverse momentum,  $P_T$  (**b**), and mass,  $M$  (**c**), of the virtual photon. The cross-section ratios are defined as the ratio of luminosity-corrected yields from the hydrogen and deuterium targets. Also shown (open black squares) are the results of the NuSea experiment<sup>4</sup> for the  $x_t$  dependence, with statistical uncertainties only. NuSea also reports an overall 1% common systematic uncertainty. The mass scale of the NuSea data is up to

50% larger than that of the SeaQuest data, and the distributions in the other kinematic variable,  $x_b$ , are slightly different owing to the differing beam energies and acceptances of the experiments. These differences imply that the cross-section ratios do not need to be identical. This is demonstrated by the red solid and violet dashed curves representing NLO calculations of the cross-section ratio with SeaQuest and NuSea kinematics using CT18 parton distributions<sup>29</sup>. The horizontal bars on the data points indicate the width of the bins.

(antiquarks) and gluons, beyond the minimal three-quark Fock state. These additional quarks and antiquarks are referred to as sea quarks. Collectively quarks and gluons are referred to as partons. It is not possible to identify any individual up or down quark as a sea or valence quark, but antiquarks and strange quarks must belong to the sea, so their study promises to reveal information about the structure of the proton. Even before QCD, hadronic models emphasized the importance of the presence of mesons (for example, ref.<sup>5</sup>), and therefore (as was realized later) antiquarks, in the physical state of a proton or neutron. Nevertheless, the initial naive expectation was that the sea was formed predominantly by gluons splitting into quark–antiquark pairs. Indeed, several authors assumed that at some low momentum scale the sea quarks and gluons vanish, and at high momentum scales they are all generated by gluon radiation and then gluon splitting. These assumptions were used to describe successfully the existing data in the late 1970s (for example, refs.<sup>6,7</sup>).

In the early 1990s the New Muon Collaboration (NMC) reported measurements of the deep inelastic structure functions ( $F_2$ ) of hydrogen (H) and deuterium (D)<sup>8,9</sup> at  $0.004 < x < 0.8$ . The cross-section for deep inelastic scattering measures the charge-squared-weighted sum

of the quark and antiquark distributions, in this case at an average scale of  $4 \text{ GeV}^2/c^2$  ( $c$ , speed of light in vacuum). The integrals of the parton distributions of the proton ( $p$ ) and neutron ( $n$ ) were assumed to have charge symmetry,  $\int_0^1 u_p(x) dx = \int_0^1 d_n(x) dx$ , where  $u_p(x)$  is the probability distribution of up quarks in the proton and  $d_n(x)$  is the distribution of down quarks in the neutron, with similar integrals for the other quark flavours, and nuclear effects in deuterium were assumed to be small ( $F_2^D = F_2^p + F_2^n$ ). In that case, their measurements and their estimate of the unmeasured region led NMC to conclude

$$\int_0^1 \frac{dx}{x} [F_2^p(x) - F_2^n(x)] = \frac{1}{3} + \frac{2}{3} \int_0^1 dx [\bar{u}(x) - \bar{d}(x)] = 0.235 \pm 0.026, \quad (1)$$

and thus the integral of  $\bar{d}(x)$  is greater than that of  $\bar{u}(x)$ ,

$$\int_0^1 dx [\bar{d}(x) - \bar{u}(x)] = 0.147 \pm 0.039, \quad (2)$$

where  $\bar{u}(x)$  and  $\bar{d}(x)$  are the distributions of up and down antiquarks in the proton, respectively.

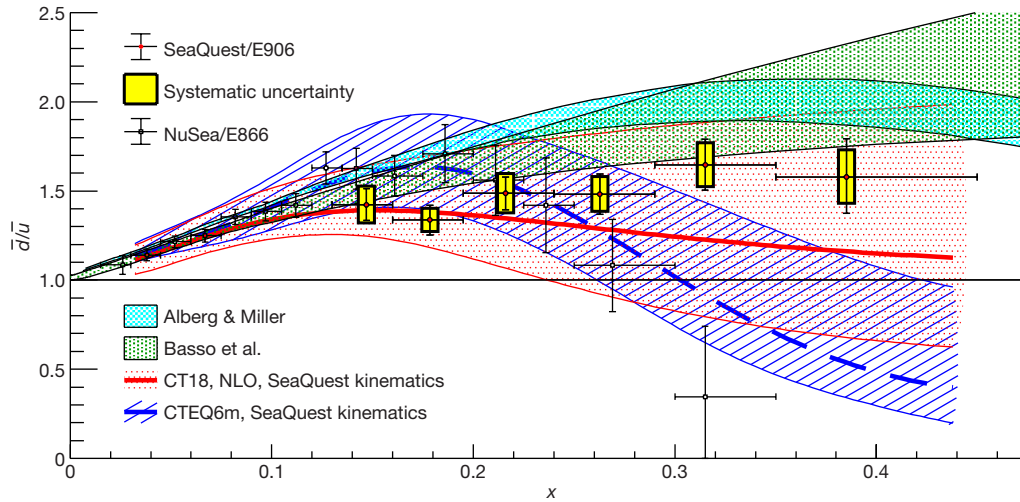


**Fig. 2 | Ratios  $\bar{d}(x)/\bar{u}(x)$ .** Ratios  $\bar{d}(x)/\bar{u}(x)$  in the proton (red filled circles) with their statistical (vertical bars) and systematic (yellow boxes) uncertainties extracted from the present data based on NLO calculations of the Drell–Yan cross-sections. Also shown are the results obtained by the NuSea experiment (open black squares) with statistical and systematic uncertainties added in quadrature<sup>4</sup>. The cyan band shows the predictions of the meson–baryon model

The Drell–Yan process in hadron–hadron collisions is a reaction in which a quark and an antiquark annihilate into a virtual photon, and that virtual photon decays into a lepton–antilepton pair<sup>10</sup>. One can isolate the antiquark distributions from the Drell–Yan cross-section by making use of this property. At lowest order, the Drell–Yan cross-section  $\sigma$  is given by

$$\frac{d^2\sigma}{dx_b dx_t} = \frac{4\pi\alpha^2}{9s x_b x_t} \sum_q e_q^2 [q(x_b)\bar{q}(x_t) + \bar{q}(x_b)q(x_t)], \quad (3)$$

where  $x_b$  and  $x_t$  are the momentum fractions of the beam and target partons participating in the reaction, respectively,  $e_q$  is the electrical charge of quark flavour  $q$ ,  $q(x)$  and  $\bar{q}(x)$  are the probability distributions for quarks and antiquarks of flavour  $q$  in the proton,  $\alpha$  is the fine-structure constant, and  $s$  is the square of the centre of mass energy of the beam and target. In a Drell–Yan measurement at CERN, the NA51 collaboration confirmed<sup>11</sup> that  $\bar{d}(x)$  is larger than  $\bar{u}(x)$  at an average  $x$  value of 0.18.

When a Drell–Yan experiment is performed with a proton beam and kinematic acceptance that selects events with  $x_b$  in the valence-quark-dominated region and with Feynman momentum fraction  $x_t = x_b - x_t \gg 0$ , the first term in equation (3) dominates. The charge-squared weighting and the fact that  $u_v(x)$  is approximately  $2d_v(x)$  for the valence quark distributions of the proton beam mean that the measurement is, by a factor of approximately eight, more sensitive to  $\bar{u}$  quarks in the target than  $\bar{d}$ . The renormalization and factorization scales for the extraction of parton distributions are usually chosen as the mass of the virtual photon squared times the speed of light squared,  $M^2c^2 = (x_b x_t s/c^2) - P_T^2$ , where  $P_T^2$  is the square of the transverse momentum of the virtual photon and is usually small compared to  $M^2c^2$ . Using charge symmetry<sup>12</sup> to relate the proton and neutron parton distributions ( $u_p(x) = d_n(x)$ ,  $d_p(x) = u_n(x)$ ,  $\bar{u}_p(x) = \bar{d}_n(x)$ ,  $\bar{d}_p(x) = \bar{u}_n(x)$ ), as is assumed by almost all the global parton distribution fits, and assuming that the nuclear corrections in the deuteron are small, as supported by calculations<sup>13,14</sup>, the ratio of the Drell–Yan cross-section on a deuterium target to that on a hydrogen target,  $\sigma_D/\sigma_H \approx (\sigma_p + \sigma_n)/\sigma_p \approx 1 + [\bar{d}_p(x_t)/\bar{u}_p(x_t)]$ , almost directly measures  $\bar{d}(x_t)/\bar{u}(x_t)$ .

The Fermilab NuSea/E866 collaboration<sup>4</sup> (whose results are displayed in Figs. 1, 2) was able to measure the  $x_t$  dependence of the  $\sigma_D/(2\sigma_H)$  ratio

of Alberg & Miller<sup>25</sup> and the green band shows the predictions of the statistical parton distributions of Basso et al.<sup>21</sup>. The red solid (blue dashed) curves show the ratios  $\bar{d}(x)/\bar{u}(x)$  calculated with CT18<sup>29</sup> (CTEQ6<sup>35</sup>) parton distributions at the scales of the SeaQuest results. The horizontal bars on the data points indicate the width of the bins.

with an 800-GeV proton beam in the kinematic range  $0.015 < x_t < 0.35$ , and by extrapolating the results to  $x_t = 0$  and  $x_t = 1$  obtained a value of  $\int_0^1 dx [\bar{d}(x) - \bar{u}(x)] = 0.118 \pm 0.012$  at an average scale of  $54 \text{ GeV}^2/c^2$ . The HERMES collaboration also measured part of this integral and obtained results<sup>15</sup> consistent with those of NMC and NuSea. One feature of the NuSea results, with admittedly limited statistics, is the suggestion that the ratio of  $\bar{d}(x)/\bar{u}(x)$  begins to decrease for  $x > 0.2$ , reaching a value of  $\bar{d}(x)/\bar{u}(x) = 0.35 \pm 0.40$  at  $x = 0.31$ , as seen in Fig. 2.

There are various mechanisms that may account for the antiquark flavour asymmetry of the proton; recent reviews include refs.<sup>16,17</sup>. Pauli blocking<sup>18</sup> may lead to a flavour asymmetry as the extra  $u$  valence quark Pauli blocks some  $u-\bar{u}$  pairs from forming, but the  $x$  dependence and even the sign of this mechanism are debated in the literature<sup>3,19</sup>. A related approach involves statistical models<sup>20,21</sup>. Another class that includes chiral soliton models<sup>22</sup> and meson–baryon models emphasizes mesonic degrees of freedom in the proton structure<sup>23–25</sup>. These latter models (statistical, chiral soliton and meson–baryon) attempt to describe the entire non-perturbative composition of the proton, and a common feature of these models is a rise in the  $\bar{d}/\bar{u}$  flavour asymmetry with  $x$ . Although at low  $x$  this behaviour reproduces the NuSea data, none of these models is able to reproduce the fall-off at higher  $x$  observed by NuSea. The only ab initio technique with which to calculate the parton distributions of the proton is lattice QCD (recently reviewed by Lin et al.<sup>26</sup>). At this time, the lattice results for both quarks and antiquarks are still not in quantitative agreement with global fits of parton distributions to experimental data, and the systematic errors are still being evaluated.

The SeaQuest experiment (E906) at Fermi National Accelerator Laboratory (Fermilab) was designed to investigate the flavour asymmetry at higher  $x_t$  values than NuSea with the newly constructed experimental apparatus that is described in detail in ref.<sup>27</sup>. With a proton beam at an energy of 120 GeV, liquid hydrogen and deuterium targets and a focusing magnet of 10 T m after the target region, the experiment was optimized for the study of target antiquarks in the intermediate region, with  $x_t$  around 0.3, by detecting muon ( $\mu^+\mu^-$ ) pairs from decays of the virtual photons produced in the Drell–Yan process. The proton beam was extracted from the Fermilab Main Injector using slow-spill extraction for 4 s every 60 s. The microstructure of the beam consisted of 1-ns-long bunches of approximately 0 to 80,000 protons at 53 MHz repetition rate. About

**Table 1 | Ratios  $\sigma_D/(2\sigma_H)$** 

$x_t$ bin	$\sigma_D/(2\sigma_H) \pm \text{stat.} \pm \text{syst.}$					$\delta x_t$
0.130–0.160	0.147	0.688	4.71	0.651	$1.211 \pm 0.052 \pm 0.053$	0.013
0.160–0.195	0.179	0.611	4.88	0.717	$1.141 \pm 0.043 \pm 0.025$	0.016
0.195–0.240	0.216	0.554	5.11	0.757	$1.196 \pm 0.042 \pm 0.044$	0.019
0.240–0.290	0.263	0.519	5.46	0.786	$1.165 \pm 0.046 \pm 0.032$	0.022
0.290–0.350	0.315	0.498	5.87	0.785	$1.193 \pm 0.050 \pm 0.034$	0.026
0.350–0.450	0.385	0.477	6.36	0.776	$1.113 \pm 0.064 \pm 0.039$	0.030

Cross-section ratios  $\sigma_D/(2\sigma_H)$  binned in  $x_t$ , with their statistical (stat.) and systematic (syst.) uncertainties and the average values for the kinematic variables in each  $x_t$  bin. The cross-section ratios are defined as the ratio of luminosity-corrected yields from the hydrogen and deuterium targets. The final column is the experimental resolution in  $x_t$ , as determined by Monte Carlo simulations.

$6 \times 10^{12}$  protons were incident on the target in the 4-s-long extraction period. A Cherenkov detector, installed in the beam line, measured the number of protons for each bunch and allowed high-intensity bunches (usually greater than 64,000 protons) to be vetoed.

The data analysis procedure is described in Methods. The primary challenge in the data analysis consisted of rate-dependent effects that were exacerbated by large fluctuations in the bunch beam intensity. The average duty factor of the beam, defined as the square of the average intensity divided by the average of the intensity squared during the beam spill,  $\langle I^2 \rangle / \langle I \rangle^2$ , ranged between 20% and 40%. These intensity variations had two primary consequences: first, a variation in the track reconstruction efficiency and second, a change in the rate of accidental coincidences. Rather than trying to separate and model all the rate-dependent effects, the ratios of the yields on deuterium,  $Y_D$ , and hydrogen,  $Y_H$ , were analysed by fitting them as a function of  $x_t$  and bunch intensity,  $I$ , with a functional form. For the final analysis, the form  $\frac{Y_D(x_t, I)}{2Y_H(x_t, I)} = R_{x_t} + aI + bI^2$  was chosen based on the Akaike information criterion<sup>28</sup>. Here,  $x_t$  is the bin average of each  $x_t$  bin,  $R_{x_t}$  is the fitted cross-section ratio at zero intensity,  $\sigma_D/(2\sigma_H)$ , and  $a$  and  $b$  are constants fitted to the entire  $x_t$  range. The results from this form were compared with other functional forms, such as  $\frac{Y_D(x_t, I)}{2Y_H(x_t, I)} = R_{x_t} + (a_0 + a_1 x_t)I + (b_0 + b_1 x_t)I^2$ , and the differences between the results obtained with these two forms were taken as part of the  $x_t$ -dependent systematic error. The only other significant systematic uncertainty was related to the relative beam normalization, which had a standard deviation of 2% of the measured ratio for each point and was completely correlated over the measurements. The cross-section ratios,  $\sigma_D/(2\sigma_H)$ , defined as the ratio of luminosity-corrected yields from the hydrogen and deuterium targets, measured by SeaQuest as a function of  $x_t$ ,  $M$  and  $P_T$ , are shown in Fig. 1 and tabulated in Table 1, along with the average  $x_b$ ,  $M$ , and  $P_T$ . (The cross-section ratios values for the  $P_T$  and  $M$  plots in Fig. 1 are given in Extended Data Tables 1, 2.) The average values of  $x_t$ ,  $x_b$ ,  $M$  and  $P_T$  in each bin are the same for deuterium and hydrogen within uncertainties and are not corrected for acceptance. The statistical uncertainty on each data point is the uncertainty returned from the fit on the zero-intensity ( $R$ ) parameter, where the uncertainty of the individual ratios only included the counting uncertainties of the Drell–Yan yields on the hydrogen and deuterium targets. Because parameters  $a$  and  $b$  are fitted over all  $x_t$  bins, the statistical uncertainty is correlated by 40–70% among  $x_t$  bins. The covariance matrix is given in equation (9) in Methods. The systematic uncertainty is fully correlated among all  $x_t$  bins. The observation that both  $M$  and  $P_T$  (for all but the very highest  $P_T$  bins) distributions for deuterium and hydrogen have the same shapes helps to confirm that the acceptances are very similar for each target. Also shown in Fig. 1 are the results from NuSea<sup>4</sup> as a function of  $x_t$  and the cross-section ratio calculated at next-to-leading order (NLO) with the CT18<sup>29</sup> parton distribution. The NuSea results are at a different scale,  $54 \text{ GeV}^2/c^2$ , than the SeaQuest results,  $22\text{--}40 \text{ GeV}^2/c^2$ . The cross-section ratios depend on both  $x_b$  and  $x_t$  and, owing to the differing beam

energies and acceptances, the  $x_b$  distributions are slightly different for SeaQuest and NuSea, the effects of which are shown in Fig. 1 and Extended Data Fig. 1.

To extract  $\bar{d}(x)/\bar{u}(x)$ , NLO calculations of  $\sigma_D/(2\sigma_H)$  were carried out, starting from several NLO global fits to the parton distributions (CT10<sup>30</sup>, CT14<sup>31</sup>, CT18<sup>29</sup>, MMHT2014<sup>32</sup>). No nuclear correction for deuterium was applied, but a systematic uncertainty of  $(0.5 + 5x_t)\%$  was included according to the range of deviation from unity found in refs.<sup>13,14</sup>. Holding all other parton distributions fixed, including the sum  $\bar{d}(x) + \bar{u}(x)$ , the ratio  $\bar{d}(x)/\bar{u}(x)$  for each  $x_t$  bin was varied until the results converged on the measured cross-section ratios. The correlations of the statistical uncertainties of  $\sigma_D/(2\sigma_H)$  were propagated through the extraction of  $\bar{d}/\bar{u}$ . The dependence of the ratio  $\bar{d}(x)/\bar{u}(x)$  above the measured  $x$  region on the value of  $\sigma_D(x)/[2\sigma_H(x)]$  was estimated by varying this value from 1.0 to 0.5 and 2.0. The spread of the results due to the choice of initial parton distributions was always less than half of the statistical error. Each  $x_t$  bin was subdivided into multiple  $x_b$  sub-bins. The cross-sections for hydrogen and deuterium were calculated separately for each sub-bin at  $\langle x_t \rangle$ ,  $\langle x_b \rangle$  and  $\langle M \rangle$  of that sub-bin, and an acceptance-weighted sum was used to determine the final cross-section. These distributions are given in Extended Data Table 3. Calculations using only one average  $x_t$  and  $x_b$  for each  $x_t$  bin were less reliable. It was also found that a leading-order extraction of  $\bar{d}(x)/\bar{u}(x)$  using leading-order parton distributions and cross-section calculations gave very similar results for the ratios as the NLO results.

The resulting  $\bar{d}(x)/\bar{u}(x)$  ratios obtained when starting with the CT18 distributions are given in Table 2 at the scale of each  $x_t$  bin and are displayed in Fig. 2 in comparison with the NuSea results. The trends between the two experiments at higher  $x_t$  are quite different. No explanation has been found yet for these differences, even though there is a small overlap between the members of the NuSea and SeaQuest

**Table 2 | Ratios  $\bar{d}(x)/\bar{u}(x)$** 

	$\bar{d}(x)/\bar{u}(x) \pm \text{stat.} \pm \text{syst.}$
0.147	$1.423^{+0.089}_{-0.089} +0.104_{-0.103}$
0.179	$1.338^{+0.083}_{-0.085} +0.065_{-0.065}$
0.216	$1.487^{+0.092}_{-0.092} +0.111_{-0.110}$
0.263	$1.482^{+0.114}_{-0.113} +0.098_{-0.097}$
0.315	$1.645^{+0.144}_{-0.140} +0.125_{-0.121}$
0.385	$1.578^{+0.214}_{-0.203} +0.153_{-0.148}$

Ratios  $\bar{d}(x)/\bar{u}(x)$  with their upper and lower statistical and systematic uncertainties. The analysis was based on the present cross-section ratio data and NLO calculations of the Drell–Yan cross-sections using CT18 parton distributions for all calculations except  $\bar{d}(x)/\bar{u}(x)$ . The systematic uncertainty is fully correlated among all  $x$  bins. The systematic uncertainty does not include a contribution from the choice of the base (CT18) parton distributions, which is small if added in quadrature to the other systematic uncertainties.

collaborations. The present data are reasonably described by the predictions of the statistical parton distributions of Basso et al.<sup>21</sup> and by the chiral effective perturbation theory of Alberg & Miller<sup>25</sup>, also shown in Fig. 2. These two calculations emphasize rather different non-perturbative mechanisms that lead to the differences in  $\bar{d}(x)$  and  $\bar{u}(x)$ . The present data show that  $\bar{d}$  is greater than  $\bar{u}$  for the entire  $x$  range measured in this experiment. This provides important support for these and other non-perturbative mechanisms of the QCD structure of the proton that were disfavoured by the NuSea results.

The next major step to help us to assess the various models is to measure how much the spin and angular momentum of the antiquarks contribute to the total spin of the proton. It has long been realized that these models make rather different predictions for the contribution of the total spin of the proton carried by the antiquarks<sup>16,17</sup>. For example, meson–nucleon models predict that little spin is carried by the antiquarks, the statistical model finds a difference in spin of  $\Delta\bar{d}(x) - \Delta\bar{u}(x) = -[\bar{d}(x) - \bar{u}(x)]$ , and chiral soliton models<sup>22</sup> predict  $\Delta\bar{d}(x) - \Delta\bar{u}(x) = -\frac{5}{3}[\bar{d}(x) - \bar{u}(x)]$ . Experiments are planned or are underway at Fermilab, the Thomas Jefferson National Accelerator Facility, Brookhaven National Laboratory and the European Organization for Nuclear Research to pursue this goal<sup>16,17</sup>.

These results affect the reach of a  $p$ – $p$  collider, such as the Large Hadron Collider, for new physics. For example, production of the high-mass  $Z'$  and  $W'$  particles has been shown to be dominated by light-quark fusion<sup>33</sup>. Calculations with contrasting statistical distributions (CTEQ6 distributions), which mimic the present (NuSea) data, show that the ratio  $\bar{d}/\bar{u}$  is relatively insensitive to scale in each case. At mass scales of 4–5 TeV/ $c^2$ , just above current limits on  $Z'$  production<sup>34</sup>, cross-sections driven by the fusion of  $u_v(x_1)$  and  $\bar{d}(x_2)$  with  $x_1 \approx x_2 = 0.3$ – $0.4$  will be enhanced according to the present results, and cross-sections driven by  $u_v(x_1)\bar{u}(x_2)$  will be diminished, compared to those calculated with the central values of previous parton distributions.

## Online content

Any methods, additional references, Nature Research reporting summaries, source data, extended data, supplementary information, acknowledgements, peer review information; details of author contributions and competing interests; and statements of data and code availability are available at <https://doi.org/10.1038/s41586-021-03282-z>.

- Ji, X., Yuan, F. & Zhao, Y. Proton spin after 30 years: what we know and what we don't? *Nat. Rev. Phys.* **3**, 27–38 (2021).
- Yang, Y.-B. et al. Proton mass decomposition from the QCD energy momentum tensor. *Phys. Rev. Lett.* **121**, 212001 (2018).
- Ross, D. & Sachrajda, C. Flavour symmetry breaking in antiquark distributions. *Nucl. Phys. B* **149**, 497–516 (1979).
- Towell, R. S. et al. Improved measurement of the  $\bar{d}/\bar{u}$  asymmetry in the nucleon sea. *Phys. Rev. D* **64**, 052002 (2001).
- Fermi, E. & Marshall, L. On the interaction between neutrons and electrons. *Phys. Rev.* **72**, 1139–1146 (1947).

- Glück, M. & Reya, E. Dynamical determination of parton and gluon distributions in quantum chromodynamics. *Nucl. Phys. B* **130**, 76–92 (1977).
- Parisi, G. & Petronzio, R. On the breaking of Bjorken scaling. *Phys. Lett. B* **62**, 331–334 (1976).
- Amaudruz, P. et al. Gottfried sum from the ratio  $F_2^p/F_2^n$ . *Phys. Rev. Lett.* **66**, 2712–2715 (1991).
- Arneodo, M. et al. Reevaluation of the Gottfried sum. *Phys. Rev. D* **50**, R1–R3 (1994).
- Drell, S. D. & Yan, T.-M. Massive lepton pair production in hadron-hadron collisions at high-energies. *Phys. Rev. Lett.* **25**, 316–320 (1970); erratum **25**, 902 (1970).
- Balitsky, A. et al. Study of the isospin symmetry breaking in the light quark sea of the nucleon from the Drell-Yan process. *Phys. Lett. B* **332**, 244–250 (1994).
- Londergan, J. T. & Thomas, A. W. The validity of charge symmetry for parton distributions. *Prog. Part. Nucl. Phys.* **41**, 49–124 (1998).
- Kamano, H. & Lee, T.-S. H. Pion-exchange and Fermi-motion effects on the proton-deuteron Drell-Yan process. *Phys. Rev. D* **86**, 094037 (2012).
- Ehlers, P. J., Accardi, A., Brady, L. & Melnitchouk, W. Nuclear effects in the proton-deuteron Drell-Yan process. *Phys. Rev. D* **90**, 014010 (2014).
- Ackerstaff, K. et al. Flavor asymmetry of the light quark sea from semi-inclusive deep-inelastic scattering. *Phys. Rev. Lett.* **81**, 5519–5523 (1998).
- Chang, W.-C. & Peng, J.-C. Flavor structure of the nucleon sea. *Prog. Part. Nucl. Phys.* **79**, 95–135 (2014).
- Geesaman, D. F. & Reimer, P. E. The sea of quarks and antiquarks in the nucleon. *Rep. Prog. Phys.* **82**, 046301 (2019).
- Field, R. D. & Feynman, R. P. Quark elastic scattering as a source of high transverse momentum mesons. *Phys. Rev. D* **15**, 2590–2616 (1977).
- Steffens, F. M. & Thomas, A. W. Flavor asymmetry of the nucleon sea. *Phys. Rev. C* **55**, 900–908 (1997).
- Bourrely, C. & Soffer, J. New developments in the statistical approach of parton distributions: tests and predictions up to LHC energies. *Nucl. Phys. A* **941**, 307–334 (2015).
- Bourrely, C., Paschos, R. & Soffer, J. The Drell-Yan process as a testing ground for parton distributions up to LHC. *Nucl. Phys. A* **948**, 63–77 (2016).
- Pobylitsa, P. V., Polyakov, M. V., Goeke, K., Watabe, T. & Weiss, C. Isovector unpolarized quark distribution in the nucleon in the large- $N_c$  limit. *Phys. Rev. D* **59**, 034024 (1999).
- Thomas, A. W. A limit on the pionic component of the nucleon through SU(3) flavor breaking in the sea. *Phys. Lett. B* **126**, 97–100 (1983).
- Alberg, M. & Miller, G. A. Taming the pion cloud of the nucleon. *Phys. Rev. Lett.* **108**, 172001 (2012).
- Alberg, M. & Miller, G. A. Chiral light front perturbation theory and the flavor dependence of the light-quark nucleon sea. *Phys. Rev. C* **100**, 035205 (2019).
- Lin, H.-W. et al. Parton distributions and lattice QCD calculations: a community white paper. *Prog. Part. Nucl. Phys.* **100**, 107–160 (2018).
- Aidala, C. A. et al. The SeaQuest spectrometer at Fermilab. *Nucl. Instrum. Meth. Phys. Res. A* **930**, 49 (2019).
- Akaike, H. A new look at the statistical model identification. *IEEE Trans. Automat. Contr.* **19**, 716–723 (1974).
- Hou, T.-J. et al. New CTEQ global analysis of quantum chromodynamics with high-precision data from the LHC. *Phys. Rev. D* **103**, 014013 (2021).
- Lai, H.-L. et al. New parton distributions for collider physics. *Phys. Rev. D* **82**, 074024 (2010).
- Dulat, S. et al. New parton distribution functions from a global analysis of quantum chromodynamics. *Phys. Rev. D* **93**, 033006 (2016).
- Harland-Lang, L. A., Martin, A. D., Motylinski, P. & Thorne, R. G. Parton distributions in the LHC era: MMHT 2014 PDFs. *Eur. Phys. J. C* **75**, 204 (2015).
- Agashe, K. et al. CERN LHC signals for warped electroweak neutral gauge bosons. *Phys. Rev. D* **76**, 115015 (2007).
- Sirunyan, A. et al. Search for a  $W'$  boson decaying to a  $\tau$  lepton and a neutrino in proton-proton collisions at  $\sqrt{s} = 13$  TeV. *Phys. Lett. B* **792**, 107–131 (2019).
- Pumplin, J. et al. New generation of parton distributions with uncertainties from global QCD analysis. *J. High Energy Phys.* **7**, 012 (2002).

**Publisher's note** Springer Nature remains neutral with regard to jurisdictional claims in published maps and institutional affiliations.

© This is a U.S. government work and not under copyright protection in the U.S.; foreign copyright protection may apply 2021

## Methods

For the measurement of the  $pd$ -to- $pp$  Drell–Yan cross-section ratios, 50.8-cm-long liquid hydrogen (0.069 interaction lengths) and liquid deuterium (0.116 interaction lengths) targets and an empty target flask were used. The targets were interchanged every few minutes to substantially reduce time-dependent systematic effects.

The SeaQuest spectrometer was constructed for the measurement of muon tracks in the forward region (laboratory angles less than 0.1 rad). It is composed of two magnets and four detector stations, each consisting of fast trigger detectors and drift chambers, distributed over 25 m along the beam direction, with a 1-m-thick iron muon identification wall before the final detector station. The first magnet provided a 3.07-GeV/c transverse momentum kick between the target and the first detector station to enhance the acceptance for muon pairs resulting from the decay of high-mass virtual photons and to reduce the acceptance for the large background of low-mass (less than 4 GeV/c<sup>2</sup>) virtual photon events. It was filled with solid iron to absorb the proton beam and all other hadrons and electrons produced in either the target or this beam dump. A second magnet (with a 0.41-GeV/c transverse momentum kick) located between the first and second detector stations provided for charge and momentum measurements of the muons. The iron hadron absorber between the third and fourth stations was used to establish the identification of muons.

Opposite-sign muon pairs were combined into di-muon candidates. The muons of each candidate were tracked back through the spectrometer to find whether they emerged from a common vertex along the beam path and near the target. The resolution of the vertex location was about 30 cm along the beam direction, compared with the 170 cm separation between the target centre and the average interaction point of protons in the solid iron magnet. Events identified as coming from the target were refitted using the target-centre vertex location, and the di-muon mass,  $M$ , the longitudinal momentum in the laboratory frame,  $P_L$ , and the transverse momentum,  $P_T$ , were determined. With this information, the fractional momentum of the beam and target quarks participating in the reaction were calculated as

$$x_b = \frac{\mathbf{p}_{\text{target}} \cdot \mathbf{p}_{\text{sum}}}{\mathbf{p}_{\text{target}} \cdot (\mathbf{p}_{\text{beam}} + \mathbf{p}_{\text{target}})}, \quad (4)$$

$$x_t = \frac{\mathbf{p}_{\text{beam}} \cdot \mathbf{p}_{\text{sum}}}{\mathbf{p}_{\text{beam}} \cdot (\mathbf{p}_{\text{beam}} + \mathbf{p}_{\text{target}})}, \quad (5)$$

where  $\mathbf{p}_{\text{target}}$  and  $\mathbf{p}_{\text{beam}}$  are the four-momenta of the target and beam, respectively, and  $\mathbf{p}_{\text{sum}}$  is the sum of the four-momenta of the positive and negative muons. The prominent  $J/\psi$  peak (resolution of 0.21 GeV/c<sup>2</sup>) and the requirement that events come from the target or beam dump were used to calibrate the field integral of the solid iron magnet. The mass spectra are shown in Extended Data Fig. 3. Detailed field maps coupled with Hall probe measurements were used to calibrate the second magnet.

Various kinematic constraints were placed on the accepted events, the most important ones being the requirements for the virtual photon mass to be greater than 4.5 GeV/c<sup>2</sup> and for the primary vertex to be in the target region. The yields for each target were corrected by subtracting the appropriately weighted yield of the empty target flask. For much of the data sample, the deuterium target had a HD contamination of  $8.4\% \pm 0.4\%$  per molecule and the yields were corrected accordingly. The beam normalization and the uncertainty in the rate-dependence corrections were the dominant systematic errors. Other smaller contributions include the uncertainty in the purity of the deuterium target, uncertainties in the target density, and the contribution of the tail of the  $J/\psi$  and  $\psi'$  peaks to the di-muon mass spectrum above 4.5 GeV/c<sup>2</sup>.

Instantaneous fluctuations in the beam intensity during data collection presented the main challenge in the data analysis.

These fluctuations occurred at the accelerator frequency of 53 MHz and led to a luminosity-normalized rate-dependent variation in the yield of events from the deuterium and hydrogen targets for a number of different sources. Several approaches were considered to account for this variation. Generally, the simplest approach would be to reject any event produced when the accelerator was above a certain, arbitrary (fairly low) threshold, and absorb the remainder of the effect into a systematic uncertainty. This would have a substantial impact on the statistical significance of the data. A second approach would be to model each individual effect in Monte Carlo, then parameterize individual effects, and finally apply the combined parameterizations to the data. The systematic uncertainty would need to account for the accuracy of the model and for any still unknown effects. For the present data, a third method was chosen, which allowed the full statistical power of the data to be maintained without requiring each and every effect of the intensity variation to be modelled.

This method considers only the final result—the ratio of event yields between the two targets—as a function of intensity. For each  $x_t$  bin, the cross-section ratio was plotted as a function of the instantaneous beam intensity when that event occurred, as illustrated in Extended Data Fig. 2. The effect of the intensity dependence on the final result could then be parameterized from the measured data and then extrapolated to zero intensity. The simplicity of this method is that only the data are used to measure and correct for the intensity dependence. Because the  $x_t$  bin boundaries are arbitrary relative to the beam intensity, a smooth, common parameterization for the intensity dependence is to be expected. A variety of parametric forms were compared to the data. One such form is

$$\frac{Y_D(x_t, I)}{2Y_H(x_t, I)} = R_{x_t} + aI + bI^2, \quad (6)$$

where  $Y_{D(H)}$  is the luminosity-normalized, empty-target-subtracted yield of events from the deuterium (hydrogen) target. In this form,  $a$  and  $b$  are parameters of the fit that are common to all  $x_t$  bins describing the intensity,  $I$ , dependence, and  $R_{x_t}$  is the zero-intensity intercept for that bin. The intercepts resulting from the simultaneous fit of all  $x_t$  bins gives the cross-section ratio  $\sigma_b/(2\sigma_H)$  for each bin. The common intensity parameters,  $a$  and  $b$ , correlate  $\sigma_b/(2\sigma_H)$  for all bins and are also determined in the simultaneous fit. Other forms were also studied, including, for example,

$$\frac{Y_D(x_t, I)}{2Y_H(x_t, I)} = R_{x_t} + (a_0 + a_1 x_t)I + (b_0 + b_1 x_t)I^2, \quad (7)$$

which allows for an  $x_t$ -correlated intensity dependence. An example of a less conventional extrapolation form that was considered is

$$\frac{Y_D(x_t, I)}{2Y_H(x_t, I)} = R_{x_t} \cos\left(\frac{I}{a_0 + a_1 x_t}\right). \quad (8)$$

In addition, constraining either  $a$  or  $b$  to zero and thus eliminating the  $I$  or  $I^2$  dependence was explored. Using the Akaike information criterion to avoid over-parameterization, the form given in equation (6) was chosen for the extrapolation. The resulting fits from three representative  $x_t$  bins are shown in Extended Data Fig. 2. A comparison with a fit to the parameterization in equation (7) was used to estimate the systematic uncertainties. The covariance matrix for the intercepts  $R_{x_t}$  resulting from the fit to equation (6) is

$$\begin{pmatrix} 2.70 & 1.19 & 1.15 & 1.20 & 1.09 & 1.16 \\ 1.19 & 1.87 & 1.25 & 1.31 & 1.19 & 1.26 \\ 1.15 & 1.25 & 1.79 & 1.25 & 1.15 & 1.21 \\ 1.20 & 1.31 & 1.25 & 2.14 & 1.20 & 1.27 \\ 1.09 & 1.19 & 1.15 & 1.20 & 2.49 & 1.16 \\ 1.16 & 1.26 & 1.21 & 1.27 & 1.16 & 4.06 \end{pmatrix} \times 10^{-3}. \quad (9)$$



The same technique was independently applied to the data binned in transverse momenta,  $P_T$ , and mass,  $M$ .

The cross-section ratios shown in Fig. 1 and listed in Table 1 are not corrected for acceptance. To compare any calculation with the present data, it is necessary to consider the SeaQuest spectrometer's acceptance in  $x_b$ . The appropriate theoretical cross-section ratio may be calculated for a  $x_t$  bin  $i$  as

$$\left( \frac{\sigma_D}{2\sigma_H} \right)_i = \frac{\sum A_{ij} \sigma_D^{\text{calc}}(x_t, x_b, M)}{2 \sum A_{ij} \sigma_H^{\text{calc}}(x_t, x_b, M)}, \quad (10)$$

where the subscript  $j$  denotes the  $j$ th  $x_b$  sub-bin of the  $i$ th  $x_t$  bin, and  $A_{ij}$  is the acceptance for that bin, tabulated in Extended Data Table 3. Finally,  $\sigma_{D(H)}^{\text{calc}}(x_t, x_b, M)$  is the calculated cross-section, where the dependence on  $x_t$ ,  $x_b$  and  $M$  has been made explicit. The code used by SeaQuest for the NLO calculation of  $\sigma_{D(H)}^{\text{calc}}(x, M)$  was provided by W. K. Tung of CTEQ.

## Data availability

Raw data were generated at the Fermi National Accelerator Laboratory. Derived data supporting the findings of this study are available from the corresponding author upon request.

**Acknowledgements** We thank G. T. Garvey for contributions to the early stages of this experiment. We also thank the Fermilab Accelerator Division and Particle Physics Division for their support of this experiment. This work was performed by the SeaQuest Collaboration, whose work was supported in part by the US Department of Energy under grants DE-AC02-06CH11357, DE-FG02-07ER41528, DE-SC0006963; the US National Science Foundation under grants PHY 0969239, PHY 1306126, PHY 1452636, PHY 1505458, PHY 1614456; the DP&A and ORED at Mississippi State University; the JSPS (Japan) KAKENHI through grant numbers 21244028, 25247037, 25800133; the Tokyo Tech Global COE Program, Japan; the Yamada Science Foundation of Japan; and the Ministry of Science and Technology (MOST), Taiwan. Fermilab is operated by Fermi Research Alliance, LLC, under contract number DE-AC02-07CH11359 with the US Department of Energy.

**Author contributions** P.E.R. and D.F.G. are the co-spokespersons for the experiment. The entire SeaQuest Collaboration constructed the experiment and participated in the data collection and analysis. Substantial contributions to the cross-section ratio analysis were made by graduate students J.D., B.K., R.E.M., S.M., D.H.M., K. Nagai, S.P., F.S., M.B.C.S. and A.S.T. The development of the technique of extrapolation to zero intensity greatly benefited from the work of A.S.T. All authors reviewed the manuscript.

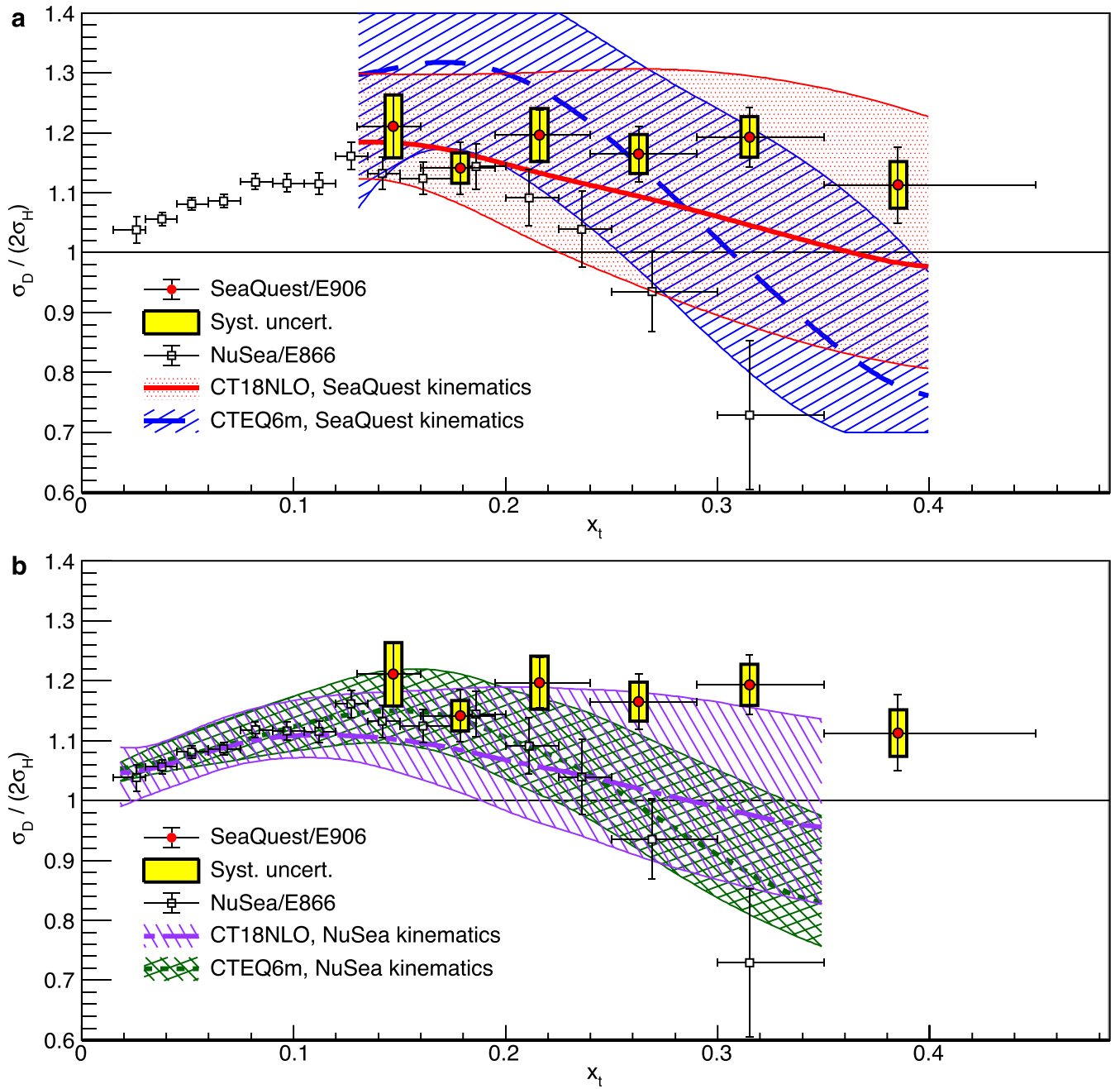
**Competing interests** The authors declare no competing interests.

## Additional information

**Correspondence and requests for materials** should be addressed to P.E.R.

**Peer review information** Nature thanks Gerald Miller, Gunar Schnell and the other, anonymous, reviewer(s) for their contribution to the peer review of this work.

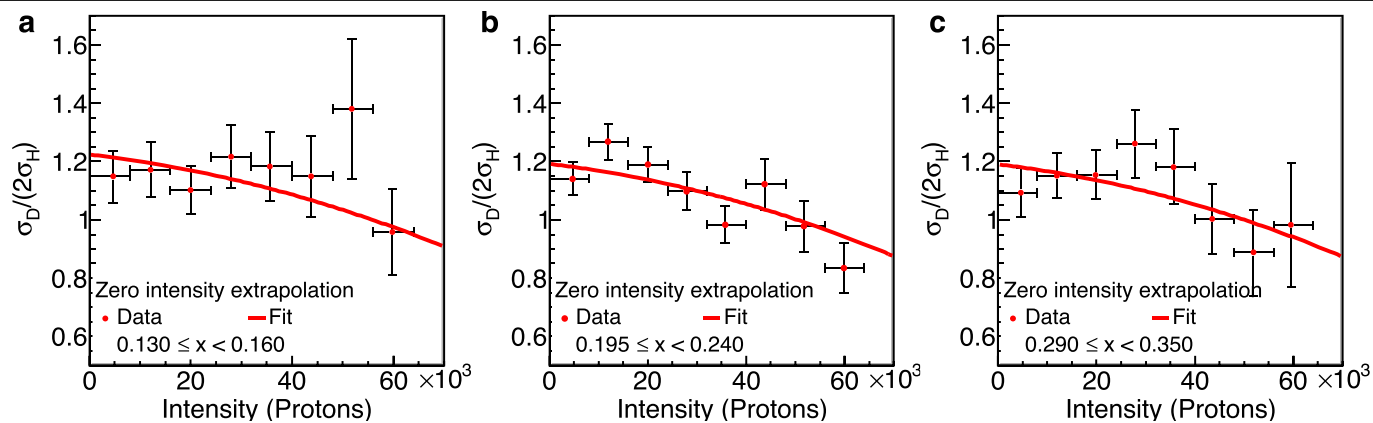
**Reprints and permissions information** is available at <http://www.nature.com/reprints>.



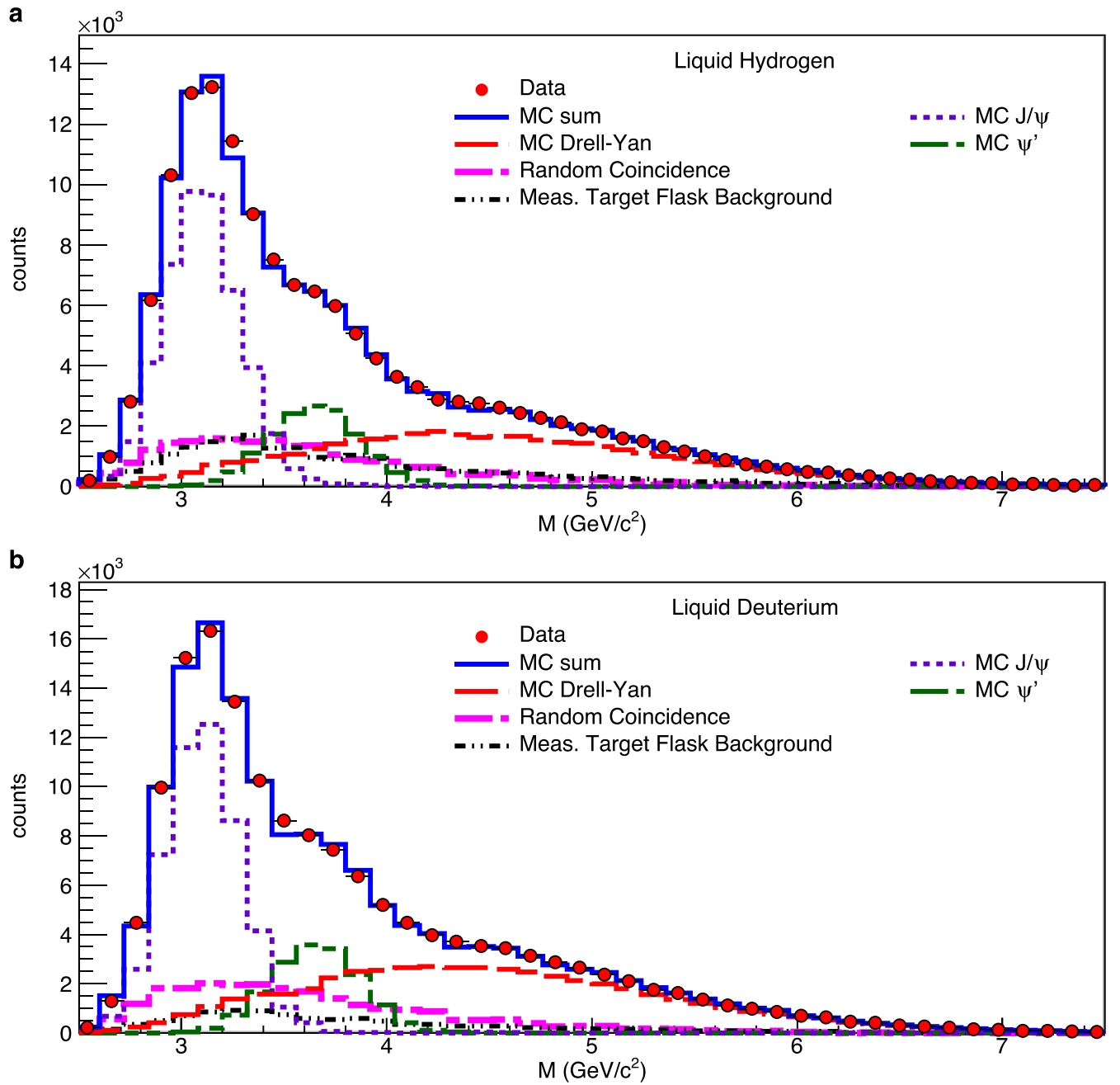
**Extended Data Fig. 1 | Comparison of NuSea and SeaQuest data with NLO calculations.** **a, b,** Comparison of the data from the present work and the NuSea measurements with NLO calculations made at the integrated kinematics of SeaQuest (**a**) and average kinematics of NuSea (**b**) based on the CT18 and CTEQ6m parton distributions. Events in the SeaQuest data were produced by a 120-GeV proton beam, whereas in the NuSea data were from an 800-GeV beam. In addition, the spectrometers, although similar in concept, had different acceptances. As a consequence, the cross-section ratios, which convolve  $x_t$

with  $x_b$ , are expected to differ because of their distinct distributions in accepted  $x_b$ . These kinematic effects can clearly be seen by the difference between the curves. Because an acceptance table analogous to Extended Data Table 3 was not available for NuSea, those calculations used  $\langle x_t \rangle$ ,  $\langle x_b \rangle$  and  $\langle M \rangle$  of the NuSea data. Both CTEQ6m and CT18 have included the NuSea data in their global analysis, so calculations based on those probability distribution functions are expected to agree better with the NuSea data. The red (violet) curve in **a** (**b**) is the same as that in Fig. 1a and is repeated here for comparison.





**Extended Data Fig. 2 | Extrapolation to zero intensity.** Extrapolation to zero intensity fits for representative  $x_i$  bins ( $0.13 \leq x_i < 0.16$  (a),  $0.195 \leq x_i < 0.240$  (b) and  $0.290 \leq x_i < 0.350$  (c)). The  $I$  (intensity) and  $P$  coefficients are common to all bins.  $\chi^2/\text{d.o.f.} = 38.7/40$  for the simultaneous fit of all  $x_i$  bins (d.o.f., degrees of freedom).



**Extended Data Fig. 3 | Reconstructed invariant mass spectra.**

**a, b,** Reconstructed muon-pair invariant-mass spectra for the liquid hydrogen (**a**) and liquid deuterium (**b**) targets. In the lower mass region, the predominant signal is produced by  $J/\psi \rightarrow \mu^+ \mu^-$  decay, followed by  $\mu^+ \mu^-$  decay of  $\psi'$ . The prominence of the  $J/\psi$  peak provides a calibration point for the absolute field of the solid iron magnet. At invariant masses above 4.5 GeV/ $c^2$ , the Drell-Yan

process becomes the dominant feature. The data are shown as red points. Additionally, Monte Carlo (MC) simulated distributions of Drell-Yan,  $J/\psi$  and  $\psi'$ , along with measured random-coincidence and empty-target backgrounds, are shown. The sum of these is shown in the blue solid curve labelled 'MC sum'. The normalizations of the Monte Carlo and the random background were from a fit to the data.

Extended Data Table 1 | Ratios  $\sigma_D/(2\sigma_H)$  as a function of  $P_T$

$P_T$ (GeV/c)	$\langle P_T \rangle$ (GeV/c)	$\sigma_D/(2\sigma_H) \pm \text{stat.} \pm \text{syst.}$	$\delta P_T$ (GeV/c)
0.0 – 0.3	0.198	$1.137 \pm 0.049 \pm 0.061$	0.161
0.3 – 0.5	0.405	$1.174 \pm 0.045 \pm 0.052$	0.177
0.5 – 0.7	0.599	$1.209 \pm 0.046 \pm 0.038$	0.188
0.7 – 0.9	0.797	$1.210 \pm 0.046 \pm 0.045$	0.194
0.9 – 1.2	1.035	$1.130 \pm 0.043 \pm 0.037$	0.198
1.2 – 1.5	1.330	$1.287 \pm 0.061 \pm 0.094$	0.201
1.5 – 1.8	1.625	$1.087 \pm 0.078 \pm 0.099$	0.206
1.8 – 2.3	1.915	$0.838 \pm 0.095 \pm 0.162$	0.204

Ratios  $\sigma_D/(2\sigma_H)$  with their statistical and systematic uncertainties as a function of transverse momentum,  $P_T$ . The cross-section ratios are defined as the ratio of luminosity-corrected yields from the hydrogen and deuterium targets. The final column,  $\delta P_T$ , is the experimental resolution in  $P_T$  as determined by Monte Carlo simulation.

Extended Data Table 2 | Ratios  $\sigma_D/(2\sigma_H)$  as a function of  $M$

$M \text{ (GeV/c}^2\text{)}$	$\langle M \rangle \text{ (GeV/c}^2\text{)}$	$\sigma_D/(2\sigma_H) \pm \text{stat.} \pm \text{syst.}$	$\delta M \text{ (GeV/c}^2\text{)}$
4.4 – 4.6	4.55	$1.170 \pm 0.053 \pm 0.059$	0.24
4.6 – 4.8	4.70	$1.204 \pm 0.047 \pm 0.039$	0.24
4.8 – 5.0	4.90	$1.202 \pm 0.048 \pm 0.039$	0.25
5.0 – 5.2	5.10	$1.163 \pm 0.050 \pm 0.039$	0.26
5.2 – 5.5	5.34	$1.123 \pm 0.046 \pm 0.037$	0.26
5.5 – 6.5	5.89	$1.183 \pm 0.043 \pm 0.042$	0.28
6.5 – 8.8	6.91	$1.167 \pm 0.068 \pm 0.096$	0.30

Ratios  $\sigma_D/(2\sigma_H)$  with their statistical and systematic uncertainties as a function of mass,  $M$ . The cross-section ratios are defined as the ratio of luminosity-corrected yields from the hydrogen and deuterium targets. The final column,  $\delta M$  is the experimental resolution in  $M$  as determined by Monte Carlo simulation.

Extended Data Table 3 | Spectrometer acceptance

<div><div><math>x_b</math></div><div><math>x_t</math></div></div>	0.30– 0.35	0.35– 0.40	0.40– 0.45	0.45– 0.50	0.50– 0.55	0.55– 0.60	0.60– 0.65	0.65– 0.70	0.70– 0.75	0.75– 0.80
0.130– 0.160						0.0007 0.589 0.158 4.54	0.0064 0.628 0.153 4.60	0.0175 0.675 0.148 4.68	0.0304 0.723 0.144 4.77	0.0370 0.772 0.144 4.92
0.160– 0.195				0.0007 0.489 0.191 4.56	0.0071 0.528 0.184 4.63	0.0188 0.576 0.178 4.74	0.0299 0.624 0.176 4.91	0.0366 0.673 0.176 5.09	0.0432 0.722 0.176 5.27	0.0471 0.772 0.175 5.45
0.195– 0.240		0.0001 0.394 0.235 4.55	0.0023 0.433 0.225 4.65	0.0105 0.477 0.217 4.78	0.0205 0.524 0.216 4.99	0.0298 0.574 0.215 5.21	0.0384 0.623 0.215 5.43	0.0456 0.672 0.214 5.63	0.0510 0.722 0.215 5.84	0.0557 0.772 0.214 6.04
0.240– 0.290		0.0015 0.383 0.267 4.76	0.0078 0.427 0.264 4.99	0.0176 0.475 0.263 5.24	0.0270 0.524 0.262 5.50	0.0364 0.574 0.262 5.75	0.0436 0.623 0.262 6.00	0.0499 0.672 0.262 6.24	0.0550 0.722 0.261 6.46	0.0591 0.771 0.262 6.69
0.290– 0.350	0.0002 0.341 0.324 4.95	0.0035 0.379 0.319 5.18	0.0120 0.426 0.316 5.46	0.0207 0.475 0.316 5.76	0.0298 0.524 0.316 6.05	0.0379 0.574 0.315 6.33	0.0455 0.623 0.315 6.60	0.0518 0.673 0.315 6.85	0.0544 0.722 0.314 7.10	0.0568 0.771 0.314 7.34
0.350– 0.450	0.0006 0.339 0.384 5.38	0.0052 0.377 0.390 5.72	0.0125 0.425 0.386 6.04	0.0203 0.474 0.386 6.38	0.0268 0.524 0.385 6.69	0.0336 0.573 0.384 7.00	0.0374 0.623 0.384 7.29	0.0405 0.672 0.384 7.58	0.0415 0.722 0.383 7.85	0.0413 0.771 0.382 8.11

The acceptance relative to a 4 $\pi$  detector and average kinematic values for bins in  $x_t$  and  $x_b$ . Each cell shows, from top to bottom, the acceptance,  $\langle x_b \rangle$ ,  $\langle x_t \rangle$  and average mass for each sub-bin.